electronic reprint

Journal of
Synchrotron Radiation
ISSN 0909-0495

Magnetic X-ray absorption fine structure for Ni–Mn alloys

T. Miyanaga, T. Okazaki, R. Maruko, K. Takegahara, S. Nagamatsu, T. Fujikawa, H. Kon and Y. Sakisaka

Copyright © International Union of Crystallography

Author(s) of this paper may load this reprint on their own web site provided that this cover page is retained. Republication of this article or its storage in electronic databases or the like is not permitted without prior permission in writing from the IUCr.

Magnetic X-ray absorption fine structure for Ni–Mn alloys

T. Miyanaga,[a]* T. Okazaki,[a] R. Maruko,[a] K. Takegahara,[a] S. Nagamatsu,[b] T. Fujikawa,[b] H. Kon[a] and Y. Sakisaka[a]

[a]Faculty of Science and Technology, Hirosaki University, Hirosaki Aomori 036-8561, Japan, and [b]Graduate School for Science, Chiba University, Yayoi, Inage, Chiba 263-8522, Japan. E-mail: takaf@cc.hirosaki-u.ac.jp

Magnetic X-ray absorption fine-structure (XAFS) spectra have been measured for Ni–Mn alloys. The magnetic XAFS in the near-edge region (X-ray absorption near-edge structure, XANES) and X-ray magnetic circular dichroism (XMCD) of the Mn and Ni *K*-edge for $Ni_{1-x}Mn_x$ (x = 0.25, 0.24 and 0.20) show that (i) the local magnetic structure around the Mn atom is quite different from that around the Ni atom, and (ii) the peak intensity in the magnetic XANES of the Mn *K*-edge depends on the magnetization of the sample in contrast to the Ni *K*-edge. The Mn *K*-edge magnetic EXAFS (extended XAFS) for $Ni_{0.76}Mn_{0.24}$ is also measured. The second and fourth peaks in the Fourier transform are observed to be enhanced in comparison with the non-magnetic EXAFS, indicating that the second- and fourth-shell Ni atoms are replaced by Mn atoms due to heat treatment (atomic ordering). Semi-relativistic theoretical calculation explains the observed magnetic EXAFS.

Keywords: XAFS; magnetic XAFS; XMCD; Ni–Mn alloy.

1. Introduction

The correlation between the structure and magnetism of 3*d* transition-metal alloys has long been an important topic in condensed matter physics. Among the 3*d* transition-metal alloys, the Mn-based alloys have recently attracted special attention because of their potential applications in the magnetic recording technology. A particular problem of the magnetism of transition-metal alloys is the formation of the magnetic moment on the Mn atom, since it is closely related to the structure of the alloy under study. An interesting example of such an alloy is Ni_3Mn, which forms an ordered phase of the type Cu_3Au with appropriate heat treatment. Ni_3Mn alloy can undergo the structural phase transition and the magnetic behaviour is sensitive to the atomic arrangement (Okazaki, 1995). Ordered Ni_3Mn is a typical ferromagnetic substance with $T_c \simeq 730$ K and where the local moment of the Mn atom and the Ni atom is $\sim$3.5 μ_B and $\sim$0.31 μ_B, respectively (Paoletti & Ricci, 1963). The magnetic structure in the Ni_3Mn alloy is explained as a result of ferromagnetic Ni–Ni, Ni–Mn and antiferromagnetic Mn–Mn first-nearest-neighbour (1NN) interactions and ferromagnetic Mn–Mn second-nearest-neighbour (2NN) interactions (Sato *et al.*, 1978); only the $J_{MnMn}^{(1NN)}$ interaction is antiferromagnetic. As a result, the alloy becomes a ferromagnetic material with the local magnetic moment of Mn being $\sim$3.5 μ_B. However, the values on each atom in the disordered state are not known. Cable & Child (1974) studied the magnetic moment distributions in disordered Ni_xMn_{1-x} (x = 0.80–0.95) alloys by the polarized-neutron diffuse-scattering method. They showed that the magnetic moment of an isolated Mn atom in $Ni_{0.95}Mn_{0.05}$ alloy is 3.50 μ_B at 4.2 K and that the magnetic moment decreases as the concentration of Mn increases and as the temperature increases. Two possible reasons were pointed out for the decreasing of the Mn magnetic moments: (i) the ferromagnetic component of the Mn moment vanishes by becoming randomly oriented or by becoming antiferromagnetically coupled; (ii) averaging over up-spin and down-spin magnetic configurations. They concluded that the magnetic distribution is complicated and not specifically defined by the neutron cross-section measurement. We can only say that the average magnetization is small compared with that in the ordered state of Ni_3Mn alloy. Since the neutron-scattering technique is based on the long-range order, we cannot say whether the net local moment of the Mn atom decreases or partially antiferromagnetic blocks are made under the conditions where the local moment of Mn is conserved even in the disordered state (Menshikov, 1999).

In order to study the magnetic structure in the process of the ordered–disordered transition, it is important to determine the short-range order on the atomic scale. The short-range order of Ni–Mn alloys has been studied by using extended XAFS (EXAFS) with synchrotron radiation (Nakahata *et al.*, 1995; Miyanaga, Okazaki, Ikeda & Kon, 1999; Miyanaga, Okazaki, Babanov & Ryazhkin, 1999; Ryazhkin *et al.*, 2001). However, it is generally difficult to distinguish the contribution of the Mn and Ni atoms by the conventional curve-fitting method because the k-dependence of the phase shifts and backscattering amplitudes of the Mn and Ni atoms are quite similar to each other. To overcome this difficulty, the small difference in the peak intensities between the Mn and Ni *K*-edge Fourier transforms was used for determining the short-range order (Nakahata *et al.*, 1995; Miyanaga, Okazaki, Ikeda & Kon, 1999). More recently, an inverse problem was introduced to the analyses of the EXAFS of Ni–Mn alloys (Miyanaga, Okazaki, Babanov & Ryazhkin, 1999; Ryazhkin *et al.*, 2001). On the other hand, magnetic XAFS is a powerful tool for investigating the local magnetic structures with short-range order in the alloys, using a circular-polarized X-ray beam from a synchrotron radiation source (Schutz *et al.*, 1987; Lovesey & Collins, 1996).

In this paper we study the magnetic XAFS for $Ni_{1-x}Mn_x$ alloys (x = 0.25, 0.24, 0.20) prepared by heat treatment for structure ordering. The amplitude of the *K*-edge XMCD spectrum is much smaller than that of the corresponding $L_{2,3}$-edge spectrum since the weak spin–orbit interaction in the diffuse 4*p* or photoelectron *p*-wave is one of the main sources of the effect. The interpretation of the magnetic XANES spectra is not so easy because they are related to both the electronic states and atomic structures. There are two approaches to analyzing the magnetic XANES: full relativistic band calculation (Ebert, 1992) and multiple-scattering theory (Brouder *et al.*, 1996; Nagamatsu & Fujikawa, 2001). On the other hand, the interpretation of the magnetic EXAFS is clear and direct for the study of the local magnetic structures, although the signal is much smaller than that of magnetic XANES. Recently, some theoretical approaches have been developed for the magnetic EXAFS analyses (Ankdinov & Rehr, 1995; Popescu *et al.*, 1999; Nagamatsu & Fujikawa, 2001). We apply the short- and long-range-order theoretical approaches to the magnetic XAFS analyses for the binary alloy system. In §2 we present the experimental details for the magnetic XANES and the magnetic EXAFS measurements. In §3 we describe the method for calculating the magnetic EXAFS and electronic structure. In §4 we first discuss the experimental results of magnetic XANES for $Ni_{1-x}Mn_x$ (x = 0.25, 0.24, 0.20) alloys, then we show the experimental results of the magnetic EXAFS for $Ni_{0.76}Mn_{0.24}$ alloy and analyze them by semi-relativistic theoretical calculations.

 © 2003 International Union of Crystallography • Printed in Great Britain – all rights reserved

electronic reprint

2. Experimental

2.1. Measurement of magnetic XANES

99.99% pure $Ni_{1-x}Mn_x$ (x = 0.25, 0.24, 0.20) alloys were prepared from an RF induction furnace. The powder samples of $Ni_{1-x}Mn_x$ (x = 0.25, 0.24, 0.20) were annealed for 140 h at 693 K under an Ar atmosphere in order to make certain an ordered state.

The magnetization curves for these samples were measured using a vibration sample magnetometer. The saturation magnetizations obtained from the magnetization curves at room temperature were 59 e.m.u. g^{-1} for $Ni_{0.75}Mn_{0.25}$, 55 e.m.u. g^{-1} for $Ni_{0.76}Mn_{0.24}$ and 35 e.m.u. g^{-1} for $Ni_{0.80}Mn_{0.20}$ alloys. The atomic structures were checked by X-ray powder diffraction and non-magnetic EXAFS. The short-range-order parameters for these samples were obtained from the relation between the magnetization and the X-ray diffraction peaks (Nakahata *et al.*, 1995). The powdered samples were mounted uniformly on adhesive tape for the magnetic XAFS measurements.

The K-edge magnetic XANES spectra (about 50 eV around the K-edge of Ni and Mn) were obtained in transmission mode at BL39XU at SPring-8. X-rays from a 8 GeV storage ring (current ~50 mA) were monochromated using an Si(111) double-crystal monochromator and then circularly polarized using a diamond (111) X-ray phase retarder. The synthetic diamond (111) crystal slab, 0.5 mm in thickness, was operated around the 220 reflection in transmission Laue geometry. A piezoelectric vibrator working at 40 Hz alternated between offset angles so as to produce a $\pi/4$ phase shift. The degree of polarization, P_c, was 0.99. Higher harmonics in the incident X-rays were rejected by inserting a Pt-coated Si mirror at θ = 5 mrad for both Ni and Mn K-edges. The XMCD signals were detected by ionization chambers filled with N_2 gas using a helicity-modulation technique utilizing a lock-in amplifier. The sample plane was inclined at 45° from the X-ray beam direction. A more detailed description of the experimental set-up of BL39XU is given elsewhere (Suzuki *et al.*, 1999). Measurements of the XMCD spectra were taken at room temperature under a magnetic field of about 1.2 T, which is strong enough to saturate the magnetization of the present samples.

2.2. Measurement of magnetic EXAFS

A 21 μm foil sample of $Ni_{0.76}Mn_{0.24}$ was prepared, polishing carefully and annealing for 100 h at 693 K under an Ar atmosphere in order to make certain an ordered state. The saturation magnetization of this sample was 56.4 e.m.u. g^{-1} and the proportion of the ordered state was deduced to be about 74%. Magnetic EXAFS of the Mn K-edge (6.4–7.2 keV) for the $Ni_{0.76}Mn_{0.24}$ foil was measured at BL28B of the Photon Factory, KEK (2.5 GeV), with circularly polarized X-rays that were generated by an ellipsoid multipole wiggler and monochromated using an Si(111) double-crystal monochromator (Iwazumi *et al.*, 1995; Kobayashi *et al.*, 1996). The absorption spectra were measured in transmission mode at 30 K. The XMCD signals were detected by ionization chambers filled with N_2 gas. Instead of switching the helicity of the incident photons, the applied magnetic field, about 0.6 T, which is still sufficient to saturate the magnetization of the sample, was reserved every 4 s to obtain a magnetic circular dichroism effect. The angle between the surface of the sample and applied magnetic fields was tilted by 45° along the incident beam. The absorption profiles were measured as $\mu_+(E)$ and $\mu_-(E)$ for each direction of the applied magnetic field.

3. Theory

3.1. Theory of magnetic EXAFS

The details of the present theoretical approach are discussed elsewhere (Fujikawa & Nagamatsu, 2002); a short summary is given here for the later discussion.

In the analysis of XMCD spectra, the full potential for an excited photoelectron is written as the sum of each atomic potential,

$$V(\mathbf{r}) = \sum_{\alpha} v_\alpha(\mathbf{r}_\alpha), \qquad \mathbf{r}_\alpha = \mathbf{r} - \mathbf{R}_\alpha, \tag{1}$$

where $v_\alpha(\mathbf{r}_\alpha)$ is the atomic potential at site $\alpha(\mathbf{R}_\alpha)$, which is assumed to be spherical symmetric for simplicity except for the spin–orbit (SO) coupling term. As a relativistic correction we take only the SO coupling into account in the two-spinor formula, which yields

$$v^\alpha = v_c^\alpha + v_{ex}^{\alpha\pm} + v_{pol}^{\alpha\pm} + \zeta^\alpha(r)\,\mathbf{S}^\alpha\cdot\mathbf{L}^\alpha, \tag{2}$$

where v_c^α is the Coulomb potential, $v_{ex}^{\alpha\pm}$ is the spin-dependent exchange potential and $v_{pol}^{\alpha\pm}$ is the optical potential due to many-body effects (Fujikawa *et al.*, 1998, 2000; Hatada *et al.*, 2001). The fourth term is the SO coupling potential. For light atoms, such as Mn and Ni, this term is much weaker than $v_0^\alpha = v_c^\alpha + v_{ex}^{\alpha\pm} + v_{pol}^{\alpha\pm}$.

Hereafter our attention is focused on light-element systems, and the SO coupling term can be treated as a weak perturbation, δv^α,

$$\begin{aligned} v^\alpha &= v_0^\alpha + \delta v^\alpha, \\ v_0^\alpha &= \begin{pmatrix} v_\alpha^+ & 0 \\ 0 & v_\alpha^- \end{pmatrix}, \\ v_\alpha^\pm &= v_c^\alpha + v_{ex}^{\alpha\pm} + v_{pol}^{\alpha\pm}, \\ \delta v^\alpha &= \begin{pmatrix} \delta v_\alpha^{++} & \delta v_\alpha^{+-} \\ \delta v_\alpha^{-+} & \delta v_\alpha^{--} \end{pmatrix}. \end{aligned} \tag{3}$$

The scattering Green's function, g_0^α, for the scattering potential, v_0^α, is diagonalized because it does not contribute to the spin–flip processes,

$$g_\alpha^0(\varepsilon) = \begin{pmatrix} g_\alpha^{0+} & 0 \\ 0 & g_\alpha^{0-} \end{pmatrix}, \tag{4}$$

where $g_\alpha^{0\pm}$ denotes the up (+) and down (−) spin Green's function which is written in terms of $v_\alpha^\pm$ and the kinetic energy operator T_e, $g_\alpha^{0\sigma}(\varepsilon) = (\varepsilon - T_e - v_\alpha^\sigma + i\eta)^{-1}$.

We can construct the full Green's function at site α in a 2 × 2 matrix,

$$g_\alpha = g_\alpha^0 + g_\alpha^0\delta v^\alpha g_\alpha^0 + g_\alpha^0\delta v^\alpha g_\alpha^0\delta v^\alpha g_\alpha^0 + \ldots. \tag{5}$$

As usual we can utilize the site T-matrix expansion of the full Green's function (Fujikawa, 1993),

$$g = g_A + \sum_{\alpha\neq A} g_A t_\alpha g_A + \sum_{\beta\neq\alpha\neq A} g_A t_\alpha g_0 t_\beta g_A + \ldots, \tag{6}$$

where t_α is the site T-matrix at site α which is related to v^α, $t_\alpha = v^\alpha + v^\alpha g_0 t_\alpha$, and g_0 is the free propagation and is different from g_α^0. For the randomly oriented systems considered here, the XMCD simply follows $\cos\beta\Delta T$, where $\Delta T = T(1,1) - T(-1,-1)$ and β is the angle between the X-ray incidence and the spin axis ($\|B$). In this case, the electron–photon interaction operator Δ_{m_p} is given by $\Delta_{m_p} = rY_{1,m_p}(\hat{r})$ ($m_p = -1, 0, 1$) neglecting unimportant constants, and we define $T(m_p, m_p')$ in terms of the 1s core spinor function, $|c\rangle$, and the full Green's function, g,

$$T(m_p, m_p') = -(1/\pi)\,\mathrm{Im\,Tr}\Big[\langle c|\Delta_{m_p}^* g \Delta_{m_p'}|c\rangle\Big]. \tag{7}$$

electronic reprint

Table 1
l-projected number of states within the Mn muffin-tin sphere and within the Ni sphere for Ni_3Mn.

		Total	Up	Down
Mn	3*d*	4.968	4.017	0.951
	4*s*	1.919	1.000	0.919
Ni	3*d*	8.194	4.361	3.833
	4*s*	1.919	1.0	0.919

Here Tr means the diagonal sum over the spin up and down states. Each of $T(m_p, m'_p)$ is written as the sum of atomic term $T^{(0)}$, single-scattering term $T^{(1)}$, and double-scattering term $T^{(2)}$, and so on,

$$T = T^{(0)} + T^{(1)} + T^{(2)} + \ldots. \quad (8)$$

The atomic X-ray absorption intensity $T^{(0)}$ is only important in the near-edge region (Fujikawa & Nagamatsu, 2002). Our attention is focused on the EXAFS region, and we can neglect this term. By applying the site *T*-matrix expansion, we can write the single scattering X-ray absorption intensity $T^{(1)}(m_p, m'_p)$ up to the first order of ζ which is dominated by the spin-conserved scattering processes. The lowest-order terms in the order of ζ^0 are most important in discussing the main features of the XAFS spectra. By use of a symmetry relation (Fujikawa *et al.*, 1997), these are cancelled out in $\Delta T^{(1)} = T^{(1)}(1, 1) - T^{(1)}(-1, -1)$. It is important to note that $\Delta T^{(1)}$ vanishes if both the X-ray absorbing atom *A* and the surrounding atoms α's are non-magnetic.

3.2. FLAPW band calculation

In order to calculate the electronic structure for the phase shift in the magnetic EXAFS we have performed band calculations using the full potential linearized augmented plane wave (FLAPW) method and the local density approximation (LDA) for the exchange correlation potential. For the LDA, an approximation proposed by Gunnarsson & Lundqvist (1976) is used. The scalar relativistic effects other than the spin–orbit interaction are included for all electrons. We introduce practically the muffin-tin (MT) sphere around each atom, but the potential is determined fully self-consistently over the entire crystal both inside and outside the MT spheres. The core electrons are treated as relaxed. A self-consistent potential is given from eigen states at sampling 20 **k**-points in the irreducible Brillouin zone (IBZ), calculated with the basis functions truncated at $|\mathbf{k} + \mathbf{G}_i| \leq 5.15(2\pi/a)$, where $\mathbf{G}_i$ is the reciprocal lattice vector, corresponding to 587 LAPW functions at the Γ point. To obtain a final band structure, eigen energies are calculated at 455 **k**-points in the IBZ. For the band-structure calculations, we used the programs *TSPACE* (Yanase, 1995) and *KANSAI*99.

In the calculation of the magnetic state, the starting crystal charge density is obtained by superposition of self-consistent charge densities for neutral atoms in which the Ni and Mn atoms are in the spin-polarized states; the electron configuration of Ni is $\ldots 3d^5 4s^1$ (up spin) and $\ldots 3d^3 4s^1$ (down spin), and that of Mn is $\ldots 3d^5 4s^1$ (up spin) and $\ldots 3d^0 4s^1$ (down spin).

Partial and total densities of states are calculated using a linearly energy-interpolated tetrahedron method. The number of valence electrons in the MT spheres are calculated from the partial densities of states (and listed in Table 1).

The model atomic structure for Ni_3Mn is $AuCu_3$-type simple cubic for simplicity as a first step. The space group is $Pm3m$ (#221, O_h^1) with Mn in $1a$:(0,0,0) and Ni in $3c$:$(1, \frac{1}{2}, \frac{1}{2})$. The value of the lattice constant used in the calculation is the experimental one in the well annealed Ni_3Mn sample (a = 3.586 A).

4. Results and discussion

4.1. Results in the magnetic XANES (XMCD)

Fig. 1 shows the magnetic XANES (XMCD) normalized by edge jumps of non-magnetic XANES for the Mn *K*-edges (*a*) and Ni *K*-edge (*b*) in $Ni_{0.75}Mn_{0.25}$ alloy. Each non-magnetic XANES is also shown by a dotted line. In Fig. 1(*a*) (Mn *K*-edge) we find a sharp positive peak (*A*) and negative peaks (*B*, *C*, *D*). In Fig. 1(*b*) (Ni *K*-edge) three distinct negative peaks (*E*, *F*, *G*) are observed. There is no positive peak in the Ni *K*-edge as observed in the well known XMCD spectrum for pure Ni. The three peaks (*E*, *F*, *G*) in the Ni–Mn alloys are typical structures, which can be observed in pure Ni, and they are more prominent for the Ni–Mn alloys than for pure Ni.

This result shows that the XMCD for the Mn *K*-edge is quite different from that for the Ni *K*-edge, although the XANES on both edges are similar. Magnetism in Ni–Mn alloys is considered to arise mainly from the ferromagnetic Ni_3Mn ordered phase. The local environment around an Mn atom is different from that around a Ni atom in the ordered Ni_3Mn alloy: 12 Ni atoms are located around one Mn atom; on the other hand, four Mn and eight Ni atoms are located around one Ni atom. Since the XMCD is a local probe of magnetic structures, the present result clearly shows the difference in the local magnetic structures around the Mn and Ni atoms in the Ni–Mn alloys. This result is in contrast to the previous result for Ni–Fe alloys (Sakurai *et al.*, 1995). In the case of the Ni–Fe alloys, the XMCD for both *K*-edges of Ni and Fe are quite similar: the final 4*p* states

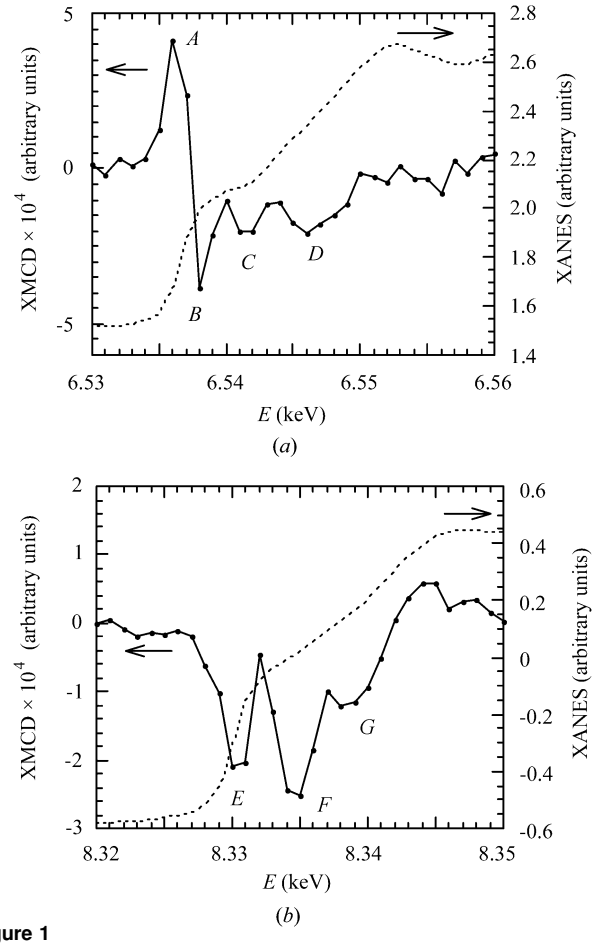

Figure 1
XMCD spectra normalized by edge jumps of non-magnetic XANES for (*a*) the Mn *K*-edge and (*b*) the Ni *K*-edge in $Ni_{0.75}Mn_{0.25}$ alloy. The dashed line represents non-magnetic XANES.

electronic reprint

hybridized with 3*d* states are not localized within a specific atom but are extended over the surrounding atoms.

Fig. 2 shows the variation of the peak intensities *A*, *B*, *C* and *D* in the XMCD for the Mn *K*-edge (*a*) and *E*, *F*, *G* for the Ni *K*-edge (*b*) as a function of the magnetization (or concentration of the Mn atom) of the sample. The peak intensity of the positive peak *A* depends on the magnetization of the sample (or the concentration of the Mn atoms). The magnetization has an influence on the peak intensity, and the sensitivity decreases as $B > C > D$. Peak *A* is more sensitive to the magnetization states of the samples than other peaks (*B*, *C*, *D*). For the Ni *K*-edge, the peak intensities of *E* and *F* are not sensitive to the magnetization. A similar result was obtained in the XMCD for Fe–Co alloys by Pizzini *et al.* (1994). They found a positive peak and negative structure at the Fe *K*-edge and only negative structure at the Co *K*-edge. The intensity of the negative peak in the Co *K*-edge XMCD decreases with Co concentration, which corresponds to an increase of the positive peak intensity in the Fe *K*-edge XMCD. In our case, Mn and Ni *K*-edge XMCD can be compared with Fe and Co XMCD in Fe–Co alloys, respectively. As the Mn concentration changes as 0.20, 0.24, 0.25, the intensity of the positive peak *A* in the Mn *K*-edge XMCD increases, but that of the negative peaks (*E*, *F*, *G*) in the Ni *K*-edge decreases.

On the band scheme, we can relate the positive peak *A* to the majority *d*-hole states near the Fermi level, which is supported by the fact that the 4*p* states are hybridized with the 3*d* states of the surrounding atoms. Within this interpretation, the decrease of the intensity of the positive peak *A* with increasing Ni concentration is in agreement with the decrease of the hole concentration of the majority *d* spin band on Mn. Pizzini *et al.* (1994) reported the increase of the magnetic moment in the Fe *d*-state as being due to the Fe concentration. Our results suggest that a *d*-hole exists only near the Fermi level (peak *A* is sensitive to the Ni concentration) and the effect of the *d* state is small (peaks *B*, *C*, *D* are not so sensitive to the concentration) in the higher-energy region as discussed previously.

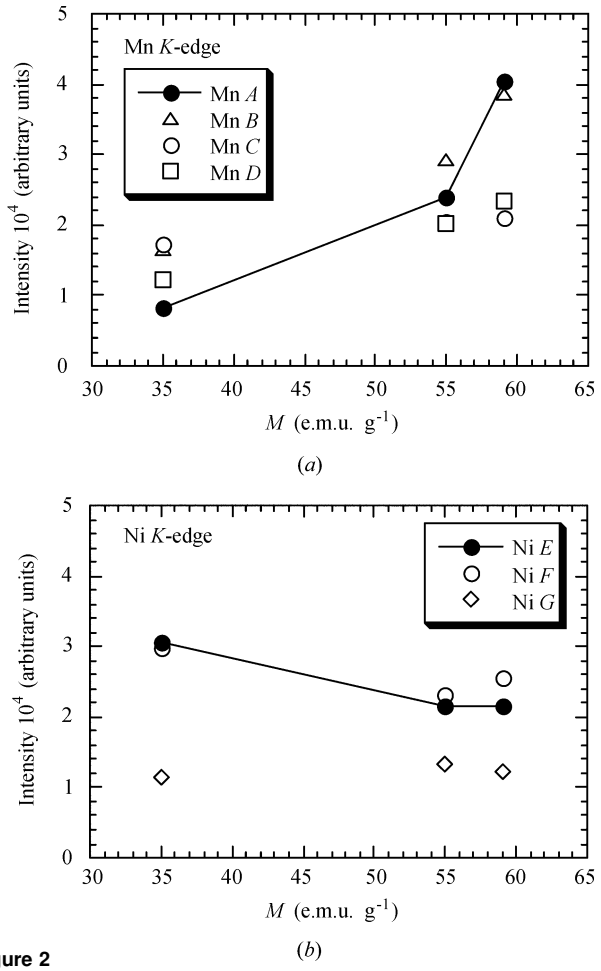

Figure 2
(*a*) Peak intensities of *A*, *B*, *C* and *D* in magnetic XANES for the Mn *K*-edge (Fig. 1*a*) as a function of the magnetization of the sample. (*b*) Peak intensities of *E*, *F* and *G* in magnetic XANES for the Ni *K*-edge (Fig. 1*b*) as a function of the magnetization.

4.2. Magnetic EXAFS for $Ni_{0.76}Mn_{0.24}$

In this section we discuss the Mn *K*-edge magnetic EXAFS for $Ni_{0.76}Mn_{0.24}$ alloy. The reason why we study this concentration is that the ordered phase of $Ni_{0.76}Mn_{0.24}$ alloy is easily obtained using a shorter heat treatment than that of $Ni_{0.75}Mn_{0.25}$ alloy. It takes longer to form ordered $Ni_{0.75}Mn_{0.25}$ alloy and so residual oxygen can oxidize the sample. Magnetic EXAFS is quite a powerful method for investigating the local magnetic structure, since this method has many advantages over the usual EXAFS technique. Recent measurements of the magnetic EXAFS have been reported for the alloys (Pizzini *et al.*, 1994) and theoretical analyses have been applied to Fe–Co and Fe–Pt alloys (Popescu *et al.*, 1999).

Fig. 3(*a*) shows the EXAFS oscillation function, $k\chi(k)$, for magnetic EXAFS (solid line) and non-magnetic EXAFS (dashed line) for the Mn *K*-edge of an $Ni_{0.76}Mn_{0.24}$ foil sample. The background subtraction is performed according to the *XANADU* code (Sakane *et al.*, 1993). The magnetic EXAFS signal is normalized by an edge jump of the non-magnetic X-ray absorption spectrum to unity. This figure shows that the magnetic EXAFS includes higher-frequency components in comparison with the non-magnetic EXAFS.

Fig. 3(*b*) shows the Fourier transforms of the EXAFS $k\chi(k)$ shown in Fig. 3(*a*). For the data analyses we used the *XANADU* code. The *k*-range of the Fourier transform is 2.0–10.8 $Å^{-1}$. The solid line (dashed line) shows the result for the magnetic (non-magnetic) EXAFS. Vertical arrows in Fig. 3(*b*) denote the crystallographic positions of nearest-neighbour atoms in the Ni–Mn f.c.c. lattice from the central Mn atom. The first-nearest-neighbour atoms are located at 2.54 Å, the second at 3.59 Å, the third at 4.5 Å and the fourth at 5.08 Å. In Fig. 3(*a*) the phase-shift correction is not considered, so the peak position is not equal to these crystallographic data. The non-magnetic EXAFS intensities simply reflect the number of surrounding atoms as previously reported (Nakahata *et al.*, 1995). On the other hand, in the magnetic EXAFS the intensity is quite different from that in the non-magnetic EXAFS. The peak intensity of the second-nearest-neighbour peak at 3.58 Å in the magnetic EXAFS is stronger than that for the first nearest neighbour at 2.54 Å in comparison with the non-magnetic EXAFS. This observation can be interpreted as follows: after the appropriate heat treatment the Ni–Mn alloys are ordered and this ordered phase mainly contributes to the magnetic circular dichroism. In the ordered phase, the Mn atoms are expected to have large magnetic moments (~3.5 μ_B from neutron diffraction) in the second shell from the Mn atom. Therefore, the second nearest Mn atoms strongly contribute to the magnetic EXAFS. On the other hand, the third-shell atoms do not contribute to the magnetic EXAFS because only Ni atoms exist as the third nearest neighbours.

Another characteristic feature is that the fourth-shell atoms give strong peaks in the magnetic EXAFS. The fourth-nearest neighbours are also Mn atoms in the ordered phase. We cannot explain the

electronic reprint

reason why the peak intensity of the fourth nearest neighbours is larger than that for the second nearest neighbours on the bases of the Cu_3Au-type ferromagnetic model. Idzerda *et al.* (1997) have reported that the higher-shell peaks are enhanced relative to the first-shell Fourier peak of the *L*-edge magnetic EXAFS for Fe, Ni and Co in comparison with the non-magnetic EXAFS. In the present case, the strong peaks for the second and fourth shell could be explained as a result of enrichment of the Mn atoms.

In order to discuss the magnetic EXAFS more quantitatively we have theoretically calculated the XMCD in the EXAFS region for the ordered f.c.c. Ni_3Mn including up to fourth-shell atoms (~5 Å) around an X-ray-absorbing Mn atom. We have detailed information on the position of the atoms by X-ray diffraction and EXAFS (Nakahata *et al.*, 1995; Miyanaga, Okazaki, Ikeda & Kon, 1999). The lattice constant a = 3.59 Å (first-nearest-neighbour distance = 2.54 Å). In order to calculate the phase shift for the magnetic EXAFS, the electronic structures were obtained from the FLAPW method. As an example of a FLAPW calculation, the density of the structure is shown in Fig. 4 and the resulting electronic states are summarized in Table 1. We used slightly modified electronic structures obtained from the FLAPW method for the phase-shifts calculation since the total charge is neutral in the Ni_3Mn system. Fig. 5(*a*) shows the calculated $k\chi(k)$ spectra of the Mn *K*-edge for the magnetic (solid line) and non-magnetic (dashed line) EXAFS. The calculated magnetic and non-magnetic EXAFS predict the main features of the experimental result shown in Fig. 3(*a*): the high-frequency component is more prominent in the magnetic than in the non-magnetic EXAFS. Fig. 5(*b*) shows the Fourier transform of $k\chi(k)$ shown in Fig. 5(*a*). The *k*-range for the Fourier transform is 2.0–10.8 $Å^{-1}$ which is the same as for Fig. 3(*b*). The amplitude of the calculated EXAFS is larger than that for the experiment, which can be explained by thermal-vibration, electron mean-free-path and many-body effects neglected in the present analyses. In the theoretical XMCD spectra the second and the fourth peaks are also enhanced in Fig. 5(*b*). This means that the 2NN and 4NN positions are replaced by Mn atoms due to the heat treatment (atomic ordering) as observed in the ordering of Ni_3Mn alloy. Actually, previous EXAFS analysis shows that the local structure around the Mn atom in ordered $Ni_{0.80}Mn_{0.20}$ is similar to that for ordered Ni_3Mn (Babanov *et al.*, 2001). On the other hand, we find a prominent discrepancy between the experimental and theoretical results at the third- and fourth-nearest-neighbour peaks. The theoretical XMCD peak intensities are in the order second > third > fourth (Fig. 5*b*). On the other hand, they are in the order fourth > second >> third (the

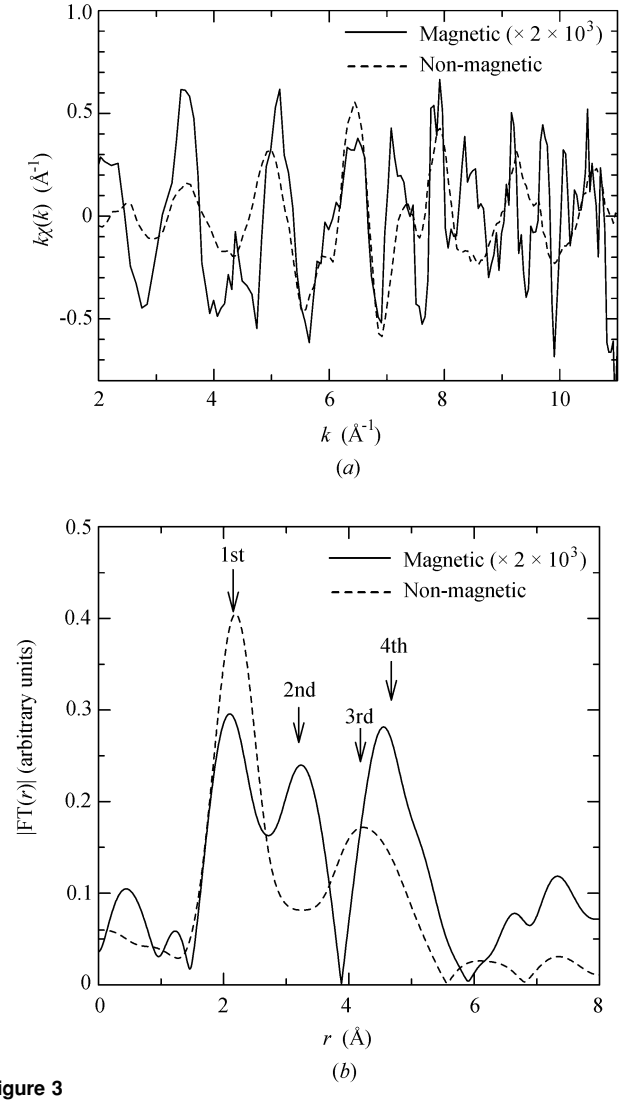

Figure 3
(*a*) EXAFS $k\chi(k)$ spectra for the Mn *K*-edge of $Ni_{0.76}Mn_{0.24}$ alloy. (*b*) Fourier transforms of the EXAFS $k\chi(k)$ spectra for the Mn *K*-edge of $Ni_{0.76}Mn_{0.24}$ alloy. The solid line represents the magnetic EXAFS and the dashed line represents the non-magnetic EXAFS.

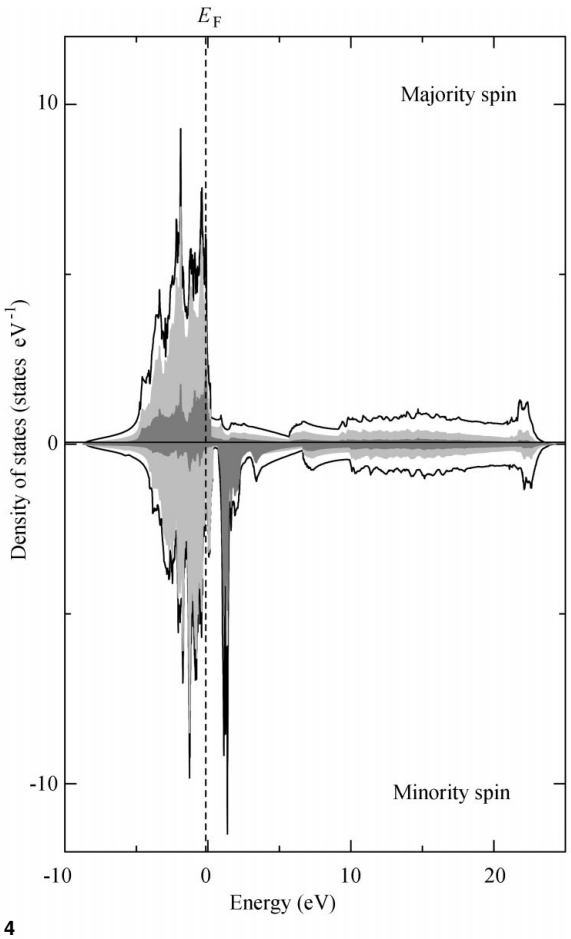

Figure 4
Total density of states (DOS) calculated by the FLAPW method for the ordered Ni_3Mn f.c.c. lattice model. The black shadow represents the states of the Mn atom, the grey shadow represents the states of the Ni atom, and the solid line represents the total contribution.

electronic reprint

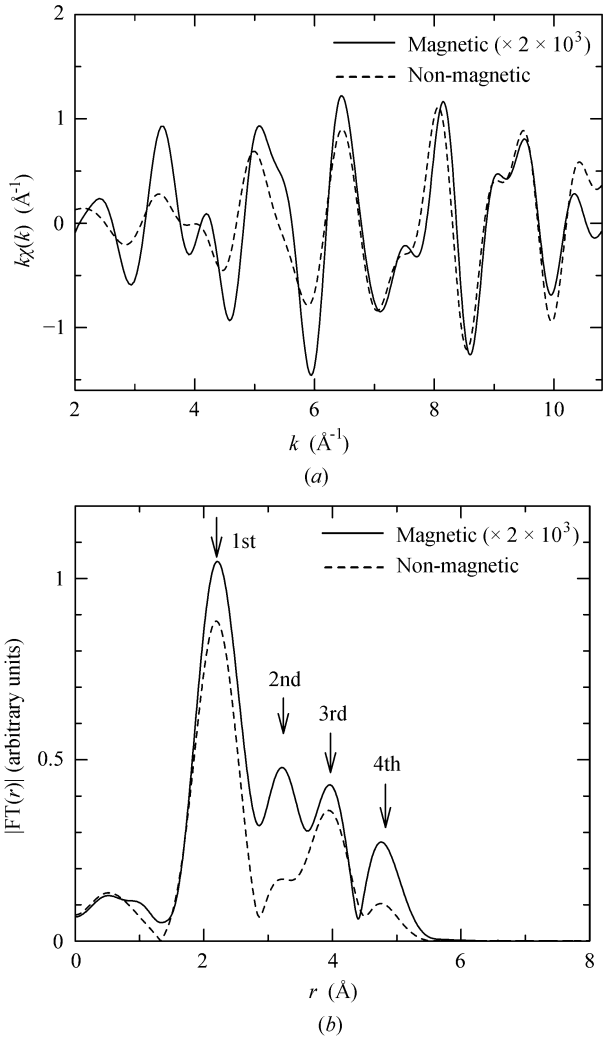

Figure 5
(*a*) Calculated EXAFS $k\chi(k)$ spectra for the Mn *K*-edge of ordered Ni_3Mn alloy. (*b*) Fourier transforms of the calculated EXAFS $k\chi(k)$ spectra for the Mn *K*-edge of the ordered Ni_3Mn alloy model. The solid line represents the magnetic EXAFS and the dashed line represents the non-magnetic EXAFS.

third peak is not observed clearly) in the experimental result (Fig. 3*b*). The following are reasons why the 4NN peak intensity is enhanced in the magnetic EXAFS:

(i) The focusing effect (or multiple scattering in the linearly arranged atoms) as observed in the normal EXAFS spectra. The peak intensity backscattered from the outer Mn atom in the Mn–Ni–Mn linear arrangement is enhanced by the photoelectron focusing effect. This effect is not taken into account in the present calculation of magnetic EXAFS.

(ii) This phenomenon is generally observed in magnetic EXAFS; however, no clear explanation has been proposed, as pointed out by Idzerda *et al.* (1997). Further systematic study is required to understand which effect is essential for the 4NN strong peaks in the magnetic EXAFS for the Ni–Mn alloy.

5. Conclusion

Magnetic XAFS spectra have been measured for Ni–Mn alloys. The XMCD of the Mn and Ni *K*-edge for $Ni_{1-x}Mn_x$ (x = 0.25, 0.24 and 0.20) show that: (i) local magnetic structure around the Mn atom is quite different from that around the Ni atom, and (ii) the peak intensity in the magnetic XANES of the Mn *K*-edge depends on the magnetization of the sample in contrast to the Ni *K*-edge. We also measured the Mn *K*-edge magnetic EXAFS for $Ni_{0.76}Mn_{0.24}$. We observed that the second and fourth peaks in the Fourier transform are enhanced in comparison with the non-magnetic EXAFS. This means that the second- and fourth-shell Ni atoms are replaced by Mn atoms due to heat treatment (atomic ordering). Semi-relativistic theoretical calculations explain well the observed magnetic EXAFS. Experimental results show that the fourth peak is more prominent than expected by the theoretical calculation. Further study is necessary to explain the characteristic features of the fourth-shell peak in magnetic EXAFS.

The authors thank Dr M. Suzuki, Professor H. Maruyama, Dr T. Iwazumi, Dr Y. Watanabe and Dr T. Nakamura for kindly supporting the measurement of the magnetic XAFS. One of the authors (TM) thanks Professor Yu. A. Babanov and Professor A. Z. Menshikov for a fruitful discussion, and Professor E. D. Crozier for encouragement of this work. This work was performed under the approval of proposal No. 1998A0280NX-np of SPring-8 and proposals Nos. 98G236 and 2001G232 of the Photon Factory.

References

Ankdinov, A. L. & Rehr, J. J. (1995). *Phys. Rev. B*, **52**, 10214–10220.
Babanov, Yu. A., Crozier, E. D., Gordon, R. A., Miyanaga, T., Okazaki, T., Pilugin, V. P. & Ryazhkin, A. V. (2001). *Nucl. Instrum. Methods Phys. Res. A*, **470**, 367–372.
Brouder, Ch., Alouani, M. & Bennemann, K. H. (1996). *Phys. Rev. B*, **54**, 7334–7349.
Cable, J. W. & Child, H. R. (1974). *Phys. Rev. B*, **10**, 4607–4615.
Ebert, H. (1992). *Jpn. J. Appl. Phys.* **32**, 299–301.
Fujikawa, T. (1993). *J. Phys. Soc. Jpn*, **62**, 2155–2165.
Fujikawa, T., Hatada, K. & Hedin, L. (2000). *Phys. Rev. B*, **62**, 5387–5398.
Fujikawa, T., Hatada, K., Yikegaki, T. & Hedin, L. (1998). *J. Electron Spectrosc. Relat. Phenom.* **88/91**, 649–655.
Fujikawa, T. & Nagamatsu, S. (2002). *Jpn. J. Appl. Phys.* **41**, 2005–2013.
Fujikawa, T., Yanagisawa, R., Yiwata, N. & Ohtani, K. (1997). *J. Phys. Soc. Jpn*, **66**, 257–262.
Gunnarsson, O. & Lundqvist, B. I. (1976). *Phys. Rev. B*, **13**, 4274–4298.
Hatada, K., Tanaka, H., Fujikawa, T. & Hedin, L. (2001). *J. Synchrotron Rad.* **8**, 210–212.
Idzerda, Y. U., Chakarian, V. & Freeland, J. W. (1997). *Synchrotron Rad. News*, **10**, 6–14.
Iwazumi, T., Koyama, A. & Sakurai, Y. (1995). *Rev. Sci. Instrum.* **66**, 1691–1693.
Kobayashi, K., Maruyama, H., Iwazumi, T. & Yamazaki, H. (1996). *Solid State Commun.* **97**, 491–496.
Lovesey, S. W. & Collins, S. P. (1996). *X-ray Scattering and Absorption by Magnetic Materials*, pp. 151. Oxford: Clarendon Press.
Menshikov, A. Z. (1999). Private communication.
Miyanaga, T., Okazaki, T., Babanov, Yu. A. & Ryazhkin, A. (1999). *Jpn. J. Appl. Phys.* S**38**, 500–503.
Miyanaga, T., Okazaki, T., Ikeda, S. & Kon, H. (1999). *J. Magn. Soc. Jpn*, **23**, 620–622.
Nagamatsu, S. & Fujikawa, T. (2001). *J. Synchrotron Rad.* **8**, 416–418.
Nakahata, M., Yuza, M., Kondo, Y., Miyanaga, T. & Okazaki, T. (1995). *J. Phys. IV*, **7**(C2), 1185–1186.
Okazaki, T. (1995). *Jpn. J. Appl. Phys.* **34**, 1537–1541.
Paoletti, A. & Ricci, F. P. (1963). *J. Appl. Phys.* **34**, 1571–1572.
Pizzini, S., Fontaine, A., Dartyge, E. C., Giorgetti, C. F., Baudelet, F., Kappler, J. P., Boher, P. & Giron, F. (1994). *Phys. Rev. B*, **50**, 3779–3788.

electronic reprint

Popescu, V., Ebert, H. & Jenkins, C. (1999). *J. Synchrotron Rad.* **6**, 711–713.
Ryazhkin, A., Babanov, Yu. A., Pilugin, V. P., Miyanaga, T., Okazaki, T., Crozier, E. D. & Gordon, R. A. (2001). *J. Synchrotron Rad.* **8**, 300–301.
Sakane, H., Miyanaga, T., Watanabe, I., Matsubayashi, N., Ikeda, S. & Yokoyama, Y. (1993). *Jpn. J. Appl. Phys.* **32**, 4641–4647.
Sakurai, H., Itoh, F., Maruyama, H., Koizumi, A., Kobayashi, K. & Yamazaki, H. (1995). *J. Phys. Soc. Jpn*, **62**, 459–463.
Sato, T., Goldfarb, R. B. & Patton, C. E. (1978). *J. Appl. Phys.* **49**, 3439–3443.
Schutz, G., Wagner, W., Wilhelm, W., Kienle, P., Zeller, R., Frahm, R. & Materlik, G. (1987). *Phys. Rev. Lett.* **58**, 737–740.
Suzuki, M., Kawamura, N., Mizumaki, M., Urata, A., Maruyama, H., Goto, S. & Ishikawa, T. (1999). *J. Synchrotron Rad.* **6**, 190–192.
Yanase, A. (1995). *Fortran Program for Space Group*, 1st ed. Tokyo: Shokabo. (In Japanese.)

Received 30 April 2002 • Accepted 6 December 2002

electronic reprint